Investigation of the Impact of Radiative Shielding by Internal Partitions Walls on Propagation of Thermal Runaway in a Matrix of Cylindrical Li-Ion Cells

Dhananjay Mishra,[1] Krishna Shah,[2,*] and Ankur Jain[1,z]

[1]*Mechanical and Aerospace Engineering Department University of Texas at Arlington, Arlington, Texas, United States of America*
[2]*Mechanical Engineering Department University of Alabama, Tuscaloosa, Alabama United States of America*

Understanding the nature of onset and propagation of thermal runaway in a Li-ion battery pack is critical for ensuring safety and reliability. This paper presents thermal runaway simulations to understand the impact of radiative heat transfer on thermal runaway onset and propagation in a pack of cylindrical Li-ion cells during transportation/storage. It is shown that radiative properties of the internal partition walls between cells commonly found in battery packs for transportation/storage play a key role in determining whether thermal runaway propagation occurs or not. Surface emissivity of the internal partitions is shown to drive a key balance between radiative heat absorbed from the trigger cell and emitted to neighboring cells. It is shown that a high thermal conductivity partition may greatly help dissipate the radiatively absorbed heat, and therefore prevent onset and propagation. Therefore, choosing an appropriate emissivity of the internal partitions may offer an effective thermal management mechanism to minimize thermal runaway. Emissivity of the cells is also shown to play a key role in radiative heat transfer within the battery pack. This work contributes towards the fundamental understanding of heat transfer during thermal runaway in a battery pack, and offers practical design guidelines for improved safety and reliability.
© 2021 The Electrochemical Society ("ECS"). Published on behalf of ECS by IOP Publishing Limited. [DOI: 10.1149/1945-7111/ac3715]

List of Symbols

C_p	specific heat capacity ($Jkg^{-1}K^{-1}$)
$\mathbf{g}$	acceleration due to gravity vector (ms^{-2})
k	isotropic thermal conductivity ($Wm^{-1}K^{-1}$)
k_r, k_θ, k_z	thermal conductivity in radial, tangential, and axial directions ($Wm^{-1}K^{-1}$)
q'''	volumetric heat generation rate (Wm^{-3})
R_u	universal gas constant ($Jmol^{-1}K^{-1}$)
R_{cyl}	radius of the cell (m)
T	temperature (K)
$\mathbf{V}$	velocity vector (ms^{-1})
α	thermal diffusivity (m^2s^{-1})
β	volumetric thermal expansion coefficient (K^{-1})
ε	hemispherical emissivity
ε_c	cell emissivity
ε_p	partition emissivity
ρ	density (kgm^{-3})
r,θ,z	Cylindrical coordinates
x,y,z	Cartesian coordinates
μ	dynamic viscosity ($kgm^{-1}s^{-1}$)

Li-ion cells and battery packs are commonly used for electrochemical energy storage and conversion. Despite favorable characteristics such as high capacity, low self-discharge rate and minimal memory effect,[1] Li-ion batteries suffer from several safety and reliability problems during operation, storage and transportation.[2] Thermal management of Li-ion battery packs is of critical importance because of the risk of thermal runaway at elevated temperatures.[3] Thermal runaway, which comprises a sequence of highly exothermic processes such as SEI decomposition, negative solvent reaction, positive solvent reaction and electrolyte decomposition reactions[4,5] can be triggered by mechanisms such as mechanical abuse,[6] electrical abuse[7,8] and thermal abuse.[9] Preventing onset of thermal runaway in a cell and preventing propagation of thermal runaway from one cell to others in the battery pack are both critical to ensure overall safety.

Extensive literature is already available on theoretical, numerical and experimental investigation of thermal runaway propagation in a battery pack. The impact of geometrical design characteristics such as cell-to-cell gap, interstitial material and location of trigger cell on thermal runaway propagation has been studied through simulations.[10,11] An experimentally validated numerical study to prevent cell-to-cell thermal runaway propagation in a battery pack showed the importance of post-venting condensation of vented gases on neighboring cells on thermal runaway propagation.[12] Investigation of thermal management design tradeoffs to prevent thermal runaway propagation has been presented.[13] The importance of insulating layer around cells and a conductive heat sink in preventing thermal runaway propagation in a Li-ion battery pack has been demonstrated.[14] The impact of state-of-charge and packing arrangement of cells on thermal runaway propagation has been studied.[15,16] Numerical study of self-heating ignition of batteries in storage has been presented.[17] A thermo-kinetic model to predict thermally-induced failure of a Li-ion cell has been developed.[18]

A number of papers on passive and active thermal management mechanisms to prevent and mitigate thermal runaway propagation are also available. An experimentally validated lumped computational model to prevent cascade propagation in the battery pack of pouch cells using cooling plates and fire walls was presented.[19] Use of 1 mm thick thermal resistant layers between adjacent batteries to prevent thermal runaway propagation is shown.[20] An experimental study on safety enhancement methods for battery module was presented with different interstitial materials. Effective suppression of thermal runaway propagation within an 11-cell 18650 battery pack was observed with graphite composite and aluminum extrusion sheet.[21] Effectiveness of a passive mitigation technique to prevent thermal runaway propagation in a battery pack was investigated with insertion of different physical barriers such as ceramic fiber, intumescent material and double layer stainless steel.[22] Prevention of thermal runaway propagation during nail penetration by using phase change composite material has been shown.[23] Battery fire suppression using a clean agent has been demonstrated.[24] Other thermal management mechanisms include water mist,[25,26] integrated PCM and micro channel cooling[27] and combined PCM and liquid cooling.[28] Studies on nonflammable electrolyte,[29] flame retardant

*Electrochemical Society Student Member.
zE-mail: jaina@uta.edu

electrolyte,[30] additives[31] and use of thermal runaway inhibitors[32] to increase thermal stability of Li-ion batteries have been reported.

Most of the thermal management techniques summarized above, including those related to thermal barriers and metal plates focus on heat removal driven by thermal conduction and/or convection, with relatively limited literature available on the effect of radiative heat transfer. High cell surface temperature during thermal runaway makes direct cell-to-cell radiation an important heat transfer mechanism, and likely to be a critical factor in determining the fate of the battery. The importance of radiative heat transfer in Li-ion cells has been noted in past work. For example, experimental measurements on LiFePO₄ pouch cells showed that 27% of the total heat exchange occurs due to radiative heat transfer.[33] In natural convection conditions, which is commonly the case for Li-ion battery packs, especially for transportation and storage, radiative heat transfer has been shown to be more significant than convective heat transfer.[34] While recognizing the importance of radiation during thermal runaway, however, there is insufficient work available on making use of available radiative heat transfer pathways to prevent thermal runaway propagation in Lithium-ion battery pack. The limited available work in this direction includes experimental results depicting improvement in tolerance of Li-ion cells to thermal abuse by virtue of radiation[35] and investigation of radiant barriers between prismatic cells in preventing thermal runaway propagation.[36]

The analysis of radiation heat transfer in the context of thermal runaway propagation may present interesting trade-offs. For example, cells with low emissivity (and hence high reflectivity) are desirable due to the reduced tendency to absorb heat and prevent thermal runaway propagation. However, high emissivity may be favorable for preventing the onset of thermal runaway in the trigger cell through radiative heat loss. Further, careful design of the radiative properties of the internal partition commonly used to separate individual cells in a matrix of cells for storage/transportation (see Fig. 1) may play an important role in preventing thermal runaway onset and propagation. Internal partitions, often made of cardboard, are already used in battery packaging, and therefore present an effective, easy-to-install and inexpensive mechanism for thermal management with minimal effect on energy density of the battery pack. There remains a critical need to investigate such radiative heat transfer-based mechanisms to enhance the thermal safety of a battery pack.

This work investigates the impact of radiative heat transfer on thermal response of Lithium Cobalt Oxide (LCO) 18650 cells during

thermal abuse scenario using finite volume simulations. In particular, the role of radiative properties of the internal partition (see Fig. 1) on onset and propagation of thermal runaway is studied. It is shown that careful choice of the radiative properties of cells as well as internal partition may help mitigate the propensity of cascade propagation in the battery pack. While high reflectivity of the cell may help prevent propagation to neighboring cells, the resulting low emissivity contributes towards thermal runaway onset in the trigger cell. Similarly, highly emissive walls of the internal partition may help in heat removal from the trigger cell. However, this may, in turn, exacerbate the safety of neighboring cells. Therefore, an optimal balance in these radiative properties may be helpful to ensure overall thermal safety and prevent thermal runaway onset and propagation in a battery pack.

Simulation Set Up

Geometry.—The simulation geometry used in this work models a typical pack of cylindrical Li-ion cells during transportation and storage. A picture of a typical pack is shown in Fig. 1a, and a schematic of the simulation geometry is shown in Fig. 1b. The geometry comprises 25 18650 Li-ion cells placed in a 5 × 5 array enclosed in a box of overall dimensions 106 mm by 106 mm by 66 mm. The cells are separated from each other using thin internal partitions of 1 mm thickness. The internal partition is typically made of wood/cardboard. The gap between each cell and internal partition is 1 mm. The overhead gap between cell top surface and the ceiling of the box is 1 mm. A heater of 1 mm thickness wrapped around the cell at the center of the pack (cell 13) provides thermal energy that triggers thermal runaway. The interstitial material around the cells is considered to be air.

Simulations carried out in this work account for multiple coupled physical phenomena, some of which may be non-linear. These include temperature-dependent heat generation due to Arrhenius decomposition reactions, surface-to-surface radiative heat transfer, anisotropic thermal conduction within cells, and natural convection within the battery pack. Modeling details pertaining to these processes are discussed in sub-sections below.

Heat generation reactions.—Heat generation in each cell in the simulations occurs as a result of four Arrhenius exothermic reactions –SEI decomposition, negative solvent reaction, positive solvent reaction, and electrolyte decomposition reaction—that are known
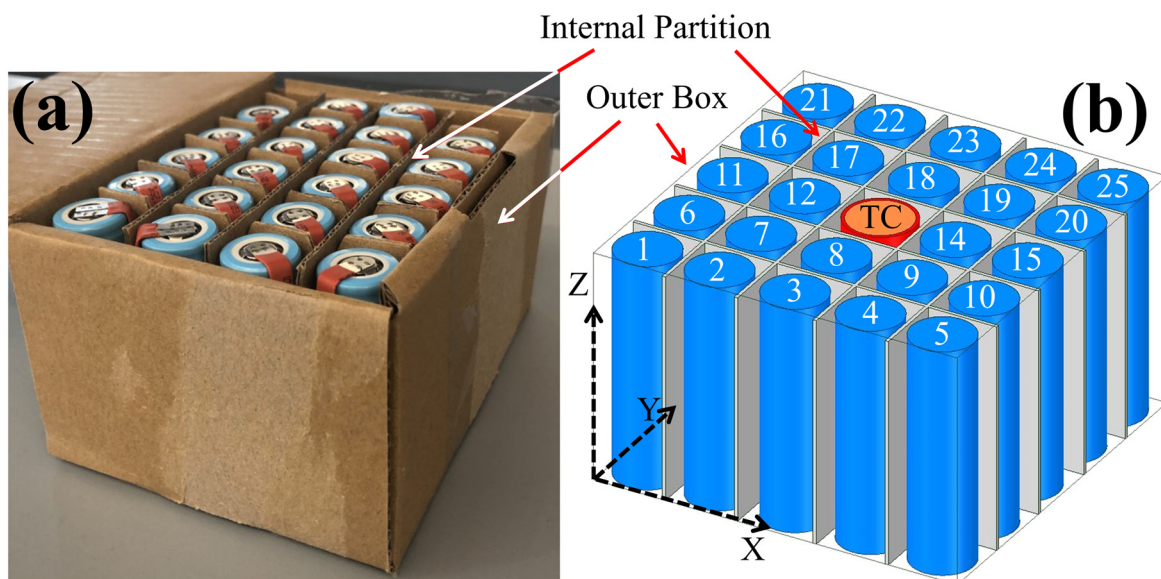
Figure 1. A pack of Li-ion cells for storage/transportation: (a) Photograph of a typical box of cells separated by internal partitions. (b) Geometry of the simulated battery pack showing 1 mm thick internal partition and trigger cell at position 13.

to occur during thermal runaway[37,38] This cascade of highly temperature-dependent heat generating reactions is triggered by Joule heating in the heater, modeled as a volumetric heat source on the cell surface. Heat generation parameter values corresponding to LiCoO$_2$ cell chemistry are assumed[37] and are described in Table I.

Thermal conduction and boundary conditions.—The governing transient thermal conduction equation for each cell is given by

$$\frac{1}{r}\frac{\partial}{\partial r}\left(k_r r \frac{\partial T}{\partial r}\right) + \frac{k_\theta}{r^2}\frac{\partial^2 T}{\partial \theta^2} + k_z \frac{\partial^2 T}{\partial z^2} + q''' = \rho c_p \frac{\partial T}{\partial t} \qquad [1]$$

Similarly, thermal conduction in interstitial and internal partition materials is written in Cartesian coordinates as

$$\frac{\partial}{\partial x}\left(\frac{\partial T}{\partial x}\right) + \frac{\partial}{\partial y}\left(\frac{\partial T}{\partial y}\right) + \frac{\partial}{\partial z}\left(\frac{\partial T}{\partial z}\right) = \frac{\rho c_p}{k}\frac{\partial T}{\partial t} \qquad [2]$$

Thermal properties of room-temperature air are assumed for the interstitial material. While internal partition materials vary widely in battery pack, a value of 0.153 Wm^{-1}K^{-1} (see Table II) representative of wooden materials, is used for the partition.

Each cell is modeled as a cylindrical orthotropic solid body with thermal conductivity values of 0.2 Wm^{-1}K^{-1}, 32 Wm^{-1}K^{-1}, and 32 Wm^{-1}K^{-1} in radial, tangential, and axial directions respectively.[39] Thermophysical properties of various materials used are listed in Table II. The outer walls of the box are subjected to a natural convection boundary condition with $h = 10$ Wm^{-2}K^{-1}, which is representative of conditions expected in transportation/storage of the battery pack. Other boundary conditions implemented include the usual no-slip boundary condition at the outer walls.

Natural convection.—Natural convection due to buoyancy of air may be important in the problem addressed here due to the large anticipated temperature rise. Heating of air in the vicinity of a hot surface results in buoyancy driven flow around cells. Natural convection is modeled through temperature-dependent density of air. The gravity vector is defined as pointing downwards (negative z direction, referring to Fig. 1b). Convective flow and heat transfer are governed by following mass, momentum and energy conservation equations:

$$\frac{\partial \rho}{\partial t} + \nabla.(\rho \mathbf{V}) = 0 \qquad [3]$$

$$\rho\left(\frac{\partial \mathbf{V}}{\partial t} + (\mathbf{V}.\nabla\mathbf{V})\right) = -\nabla.p + \mu\nabla^2\mathbf{V} + \rho\mathbf{g}\beta(T - T_\infty) \qquad [4]$$

$$\frac{\partial T}{\partial t} + \mathbf{V}.\nabla T = \alpha\nabla^2 T \qquad [5]$$

Viscous effects are neglected due to low velocity of air. Temperature-dependent change in the density of air around cells is governed by volumetric thermal expansion coefficient, β in Eq. 4. Based on the ideal gas assumption, β for air can be expressed as:

$$\beta = -\frac{1}{\rho}\frac{\Delta\rho}{\Delta T} = \frac{1}{\rho}\frac{p}{R_u T^2} = \frac{1}{T} \qquad [6]$$

Radiative heat transfer.—Radiative heat transfer in the battery pack is accounted for using surface-to-surface radiation modeling which is based on gray-diffuse model.[34] This model assumes the radiative properties of a surface to be independent of wavelength and direction. In general, a surface that is highly emissive is also highly absorptive. The total radiative heat flux for each radiating surface in the geometry being simulated is calculated, which is further used in computing the energy equation described in the previous subsection. Radiative heat transfer between any two surfaces is, in general, a function of temperature of the respective surfaces, size, relative orientation, and distance between surfaces. View factors are commonly used to characterize the impact of these parameters.[42] In

Table I. Kinetic parameters used for abuse simulations.[37]

Symbol	Description	Value
A_{sei}	SEI decomposition frequency factor	1.667×10^{15} (s^{-1})
A_{ne}	Negative-solvent frequency factor	2.5×10^{13} (s^{-1})
A_{pe}	Positive-solvent frequency factor	6.667×10^{13} (s^{-1})
A_e	Electrolyte decomposition frequency factor	5.14×10^{25} (s^{-1})
Ea_{sei}	SEI-decomposition activation energy	1.3508×10^5 (Jmol^{-1})
Ea_{ne}	Negative-solvent activation energy	13508×10^5 (Jmol^{-1})
Ea_{pe}	Positive-solvent activation energy	1396×10^5 (Jmol^{-1})
Ea_e	Electrolyte-decomposition activation energy	2.74×10^5 (Jmol^{-1})
C_{sei0}	Initial value of C_{sei}	0.15
C_{ne0}	Initial value of C_{ne}	0.75
α_0	Initial value of α	0.04
C_{e0}	Initial value of C_e	1
m_{sei}	Reaction order for C_{sei}	1
m_{ne}	Reaction order for C_{ne}	1
$m_{pe,p1}$	Reaction order for α	1
$m_{pe,p2}$	Reaction order for $(1-\alpha)$	1
m_e	Reaction order for C_e	1
$t_{sei,ref}$	Initial value of t_{sei}	0.033
H_{sei}	Sei-decomposition heat release	257 (Jg^{-1})
H_{ne}	Negative-solvent heat release	1714 (Jg^{-1})
H_{pe}	Positive-solvent heat release	314 (Jg^{-1})
H_e	Electrolyte decomposition heat release	155 (Jg^{-1})
W_c	Specific carbon content	6.104 (gm^{-3})
W_p	Specific positive active material content	1.221×10^6 (gm^{-3})
W_e	Specific electrolyte content	4.069×10^5 (gm^{-3})

Table II. Thermophysical properties of materials used for simulations.[39–41]

Material	Thermophysical properties		
	Thermal Conductivity ($Wm^{-1}K^{-1}$)	Density (kgm^{-3})	Specific heat capacity ($kJkg^{-1}K^{-1}$)
Air	0.024 (isotropic)	1.225	1.006
Li-ion cell	0.2, 32, 32 (cylindrical orthotropic)	2280	0.715
Internal Partition—wooden material	0.15 (isotropic)	700	2.6
Internal Partition—Aluminum	202.4 (isotropic)	2800	0.87

the present simulations, view factors between pairs of surfaces are calculated using ray tracing method[43] while the air between surfaces is assumed to be non-participating. All radiating surfaces are assumed to be opaque (zero transmissivity), therefore, sum of emissivity and reflectivity for each surface is unity. Radiative flux leaving a surface comprises of Stefan-Boltzmann emission by virtue of its temperature and reflected radiative flux, which depends on irradiation flux from all visible surfaces in the surroundings. The irradiation flux is the net sum of radiation energy from all surrounding surfaces participating in radiative exchange and is directly proportional to the view factors. Such surface-to-surface radiation calculations become computationally expensive due to large number of radiating surfaces. Therefore, surface clusters are created by grouping adjacent surfaces until a specified number of surfaces per cluster, five in this case, is reached. Clustering of radiating surfaces is an approximation that balances computational cost with accuracy. Radiosity, which is defined as the total radiation energy leaving a surface per unit time and per unit area is calculated for each surface cluster and these values are distributed on to the radiating faces.

In order to validate the radiation model, a special case is considered with a geometry that is representative enough of a battery pack with partitions, yet simple enough to admit an exact solution for radiation heat transfer. Specifically, a cylindrical cell of radius R surrounded by partition walls in an enclosure of size L by W is considered. The cell is offset by a distance w from the left wall. For this case, assuming all bodies are opaque black bodies, the exact analytical solution for radiative heat flux into the left wall is given by[42]

$$q''_{cyl-wall} = \frac{1}{\pi} \tan^{-1} \left[\frac{L}{2(w + R_{cyl})} \right] \sigma [T_{cyl}^4 - T_{wall}^4] \qquad [7]$$

where σ is the Stefan-Boltzmann constant.

For this scenario, Fig. 2a compares the computed radiative heat flux at the left wall with the analytical solution given by Eq. 7 as a function of R_{cyl}. Values of other geometrical parameters are $w = 300$ mm, $W = 700$ mm, $L = 400$ mm. Both cell and walls are assumed to be opaque black bodies. Figure 2b presents a similar comparison as a function of cell temperature, while holding wall temperature at 300 K. Other geometrical parameters are the same as in Fig. 2a, in addition to $R_{cyl} = 150$ mm. Both plots show excellent agreement between the radiation model and the analytical solution for this special case.

In addition, validation of other heat transfer models, such as thermal conduction and heat generation used here has been carried out by comparison with an analytical solution. More details of this comparison have been described in a recent paper.[10]

Meshing and other simulation details.—3D polyhedral mesh elements are used throughout this work. Polyhedral meshing results in each meshed element being surrounded by a greater number of elements compared to other meshing techniques, resulting in better gradient approximation. Polyhedral meshing also results in high numerical stability and low numerical diffusion. In this work, one meshed cell per gap is used for surface mesh sizing with proximity control type and three-layered boundary inflation control for each meshed cell. The maximum mesh element size is 0.05 mm, 0.1 mm and 0.5 mm for the internal partition, cells and the outer box, respectively. Contact meshing is used to enhance convergence at the intersection between the box and internal partition. The generated mesh is characterized by 1.05 growth rate and 0.33 squish index. For a 5 by 5 battery pack, upwards of 8.2 million elements are used along with a time step of 1 ms, based on a grid independence study described in the next section. Nonlinear coupled solver using implicit numerical approach with 0.001 s timestep size and 0.0001 tolerance limit is used. Convergence in these simulations is found to require 600 energy iterations per time step and 5 faces per surface cluster. Figure 3 presents representative pictures of the final mesh used in this work. Figure 3a shows a two-dimensional projection of the 3D mesh for the entire 25-cell battery pack, whereas a zoomed-in picture showing only the trigger cell, the surrounding heater and the partition walls around the trigger cell is shown in Fig. 3b.
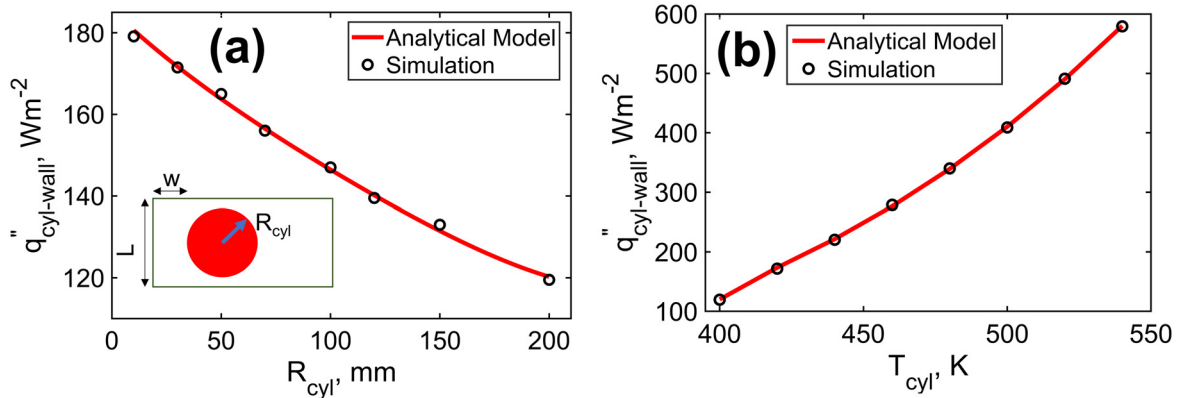
Figure 2. Validation of the radiation model: (a) Radiative heat flux between the left wall at 300 K and the cell at 400 K in an enclosure as a function of cell radius. (b) Radiative heat flux between the left wall and the cell in an enclosure as a function of cell temperature, while keeping wall temperature and cell radius at 300 K and 150 mm, respectively. Geometrical parameters are $L = 400$ mm, $W = 700$ mm, $w = 300$ mm. All bodies are assumed to be opaque, black bodies.
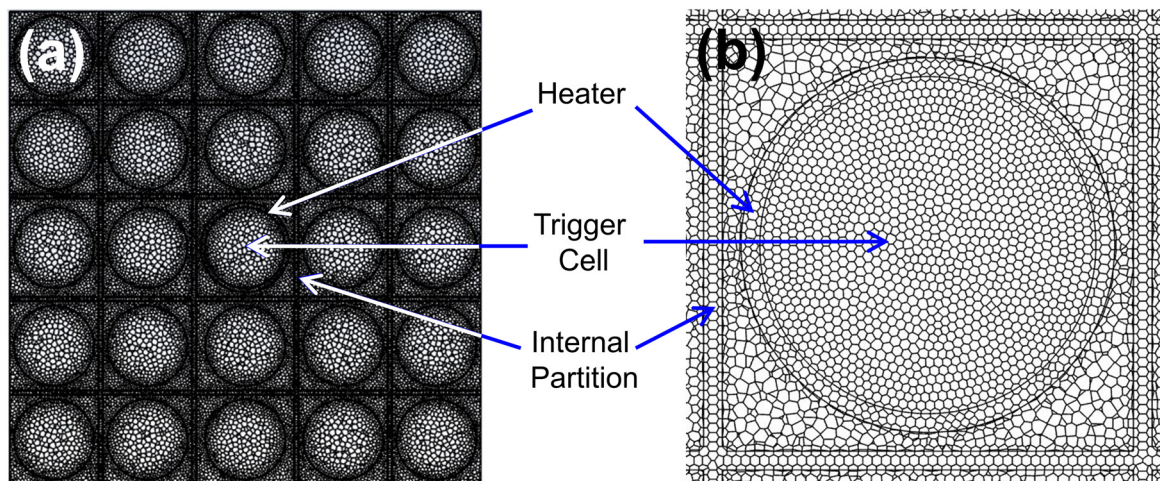
Figure 3. Pictures showing the representation mesh in cross-section view with (a) entire geometry, (b) zoomed-in to show only a small region around the trigger cell.

Note that the present work does not account for combustion of the vent gases and/or cell and partition materials. Heat spreading by advection due to vented gases is also not considered, although this has been modeled in a prior study.[11]

Results and Discussion

A multiphysics, finite-volume based computational simulation is developed to account for the physical processes described in the previous section. Validation of this general simulation framework has been carried out by comparison with an analytical solution for a simplified special case of single cell thermal abuse, as described in previous work.[10]

A number of simulations are carried out in the present work to understand the role of the internal partition and specifically its radiative properties on thermal runaway propagation in the battery pack. Table III summarizes the goals, parameter values, and key conclusions of the simulations, which are discussed in detail in this section.

The first set of simulations (Simulation A) establish timestep sensitivity of the simulations. Selection of timestep is an important tradeoff between computational efficiency and accuracy. A small timestep is preferred for smooth convergence and maintaining residuals within tolerance limit, particularly for simulations involving highly non-linear physics, such as the present case. However, a small timestep may also result in significant computational cost. In the first set of simulations, temperature distribution for the geometry described above is computed, with 8.5×10^6 Wm^{-3} heat generation in the sleeve heater up to 200 s and with three different timesteps of 10, 1 and 0.5 ms. The computed core temperatures of trigger cell (cell 13) and cell 3 are shown in Figs. 4a and 4b respectively for each case. For both cells, the predicted temperature distribution is independent of the time steps considered here. Therefore, a 1 ms fixed timestep is used for all subsequent simulations.

Similarly, grid independence study (Simulation B) is carried out to determine the minimum number of grid elements needed to ensure grid independence of results. Figures 5a and 5b plot core temperatures of trigger cell and cell 3, respectively as functions of time for three different numbers of grid elements. While there is a significant change in the computed results when the grid is refined from 4.6 to 8.2 million elements, there is much lesser change when the grid is further refined to 10.1 million elements. Between the 8.2 and 10.1 million element cases, the peak temperature and time of occurrence of the peak change by less than 3%. This shows that upwards of 8.2 million grid elements must be used to ensure accuracy of simulation results. This is a rather large number and underscores the importance

of computational optimization when carrying such non-linear simulations.
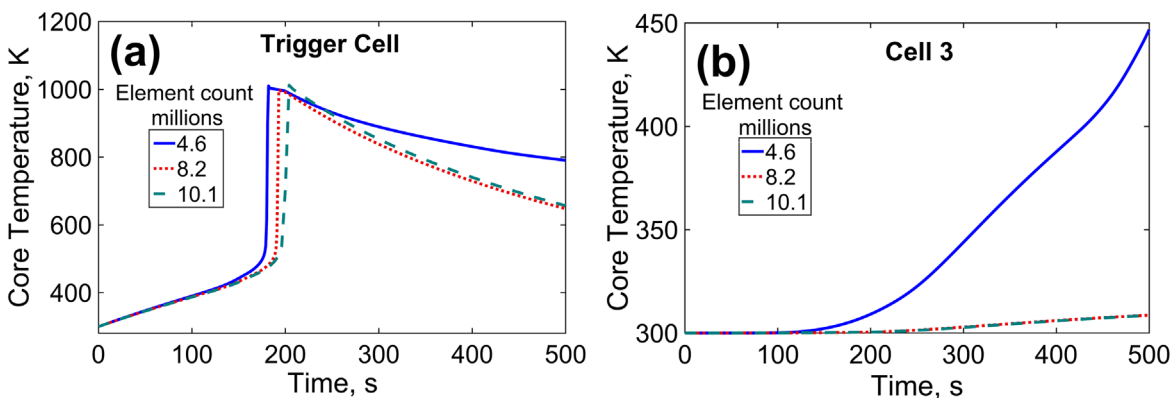
The effect of the presence of internal partition that separates each cell in the battery pack is investigated next. These simulations (Simulation C) test the hypothesis that, with appropriate radiative properties of the partition surfaces, heat generated in the trigger cell can be prevented from radiating to neighboring cells, thereby, preventing propagation. A set of simulations without and with partitions is carried out. For the simulations with partition, the partition material is assumed to be wood, with emissivity of 1.0, which may correspond to a dark-colored partition. While the intrinsic emissivity of wood/cardboard is slightly lower, the surface emissivity can be modified by paint, and an emissivity close to 1 can be obtained by painting black. The extreme case of emissivity of 1.0 is taken here to demonstrate the effect of emissivity on thermal runaway characteristics. The same values of all other parameters, such as cell-to-cell gap and reaction parameters are used in both simulations. Particularly, heat generation rate in the sleeve heater around the trigger cell responsible for onset of thermal runaway is taken to be 4.7×10^6 Wm^{-3} up to 500 s. Emissivity of each cell is taken to be 0.1, which is reasonable because cells usually have a shiny, metallic surface that is highly reflective. Simulation results are presented in Figs. 6 and 7 in the form of temperature plots and colorplots at 400 s, 800 s and 1000 s, respectively. Corresponding videos of the evolution of the temperature field over time for Simulation C (and all subsequent simulations) are available in Supplementary Information (available online at stacks.iop.org/JES/168/120507/mmedia). These videos are labeled by Simulation number and have been slowed down 0.25X for clarity. Figure 6 shows that, in the absence of the partition, neighboring cells 8 and 7 both undergo thermal runaway following the trigger cell. This is mainly due to direct radiative heat exchange between the trigger cell and its neighboring cells. In contrast, in the presence of the partition, while the trigger cell does undergo thermal runaway, there is no propagation to neighboring cells. The absence of propagation in this case is primarily due to the high emissivity (and therefore high absorptivity) of the partition walls, which absorb a significant amount of heat from the trigger cell and prevent the heat to radiatively transfer directly to the neighboring cells. In addition to the prevention of propagation to neighbors, Fig. 6b also shows delayed thermal runaway onset in the trigger cell itself compared to the baseline case (Fig. 6a), which is also due to the presence of the partition that radiatively absorbs a significant amount of heat from the trigger cell. Note that the trigger cell temperature plot in Fig. 6a shows a few inflexion points. In addition to the sharp peak corresponding to occurrence of thermal runaway, there is an

Table III. Summary of parameters and results from all simulations presented in this work.

Simulation #	To study	Figure #	Simulation Parameters				Key conclusions
			ε_p	ε_c	Partition material	Heat generation & duration (Wm^{-3}, s)	
A	Time step sensitivity	4a, 4b	0.1	0.1	Wood	8.5×10^6, (0–200)	1 ms fixed timestep is ideal for these simulations with respect to tolerance limit.
B	Grid sensitivity	5a, 5b	0.1	0.1	Wood	8.5×10^6, (0–200)	Upwards of 8.2 million elements are sufficient for 25-cell 18650 Li-ion battery pack.
C	Effect of internal partition	6, 7	1	0.1	Wood	4.7×10^6, (0–500)	Presence of internal partition prevents thermal runaway propagation.
D	Effect of internal partition material	8, 9	1, 0.1	0.1	Wood, aluminum	4.5×10^6, (0–300)	Using aluminum partition completely prevents thermal runaway onset and propagation.
E	Effect of internal partition emissivity	10, 11	0.1,1	0.1	Wood	4.5×10^6, (0–300)	Wooden partition with high emissivity significantly decreases onset and propagation probabilities of thermal runaway.
F	Effect of emissivity of cells	13, 14	0.1	1, 0.1	Wood	1.2×10^7, (0–500)	Increase in emissivity of cells delays thermal runaway propagation.
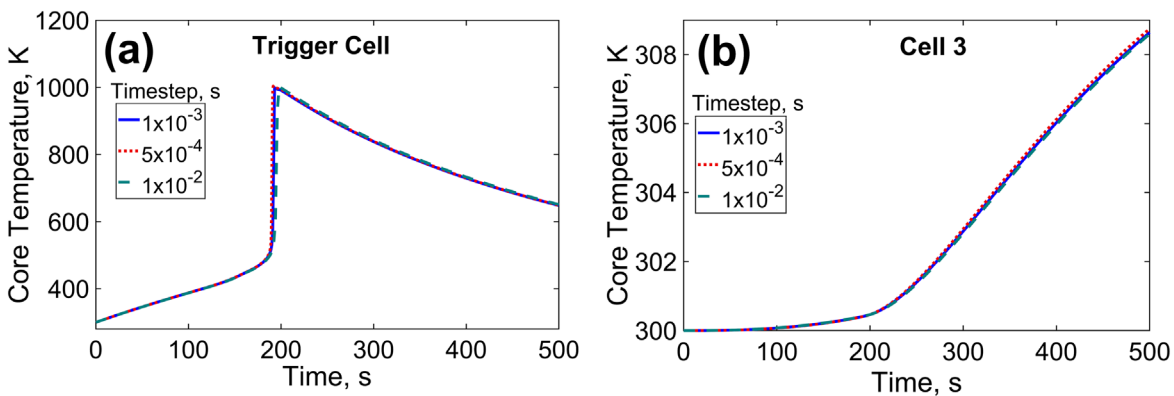
Figure 4. Simulations results to establish timestep sensitivity (Simulation A): Temperature vs time plot for (a) trigger cell, and (b) cell 3 in 5 by 5 battery pack. Problem parameters include 3 mm cell-to-cell gap, 1 mm overhead gap, 8.5×10^6 Wm^{-3} heat generation in heater up to 200 s, $\varepsilon_p = 0.1$, $\varepsilon_c = 0.1$.

Figure 5. Simulations results to establish grid sensitivity (Simulation B): Temperature vs time plot for (a) trigger cell, and (b) cell 3 in 5 by 5 battery pack. Problem parameters are the same as Fig. 4.
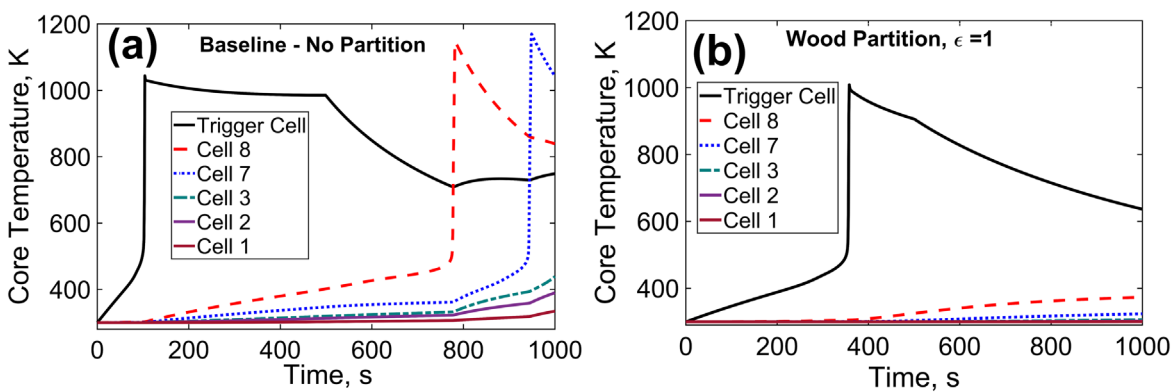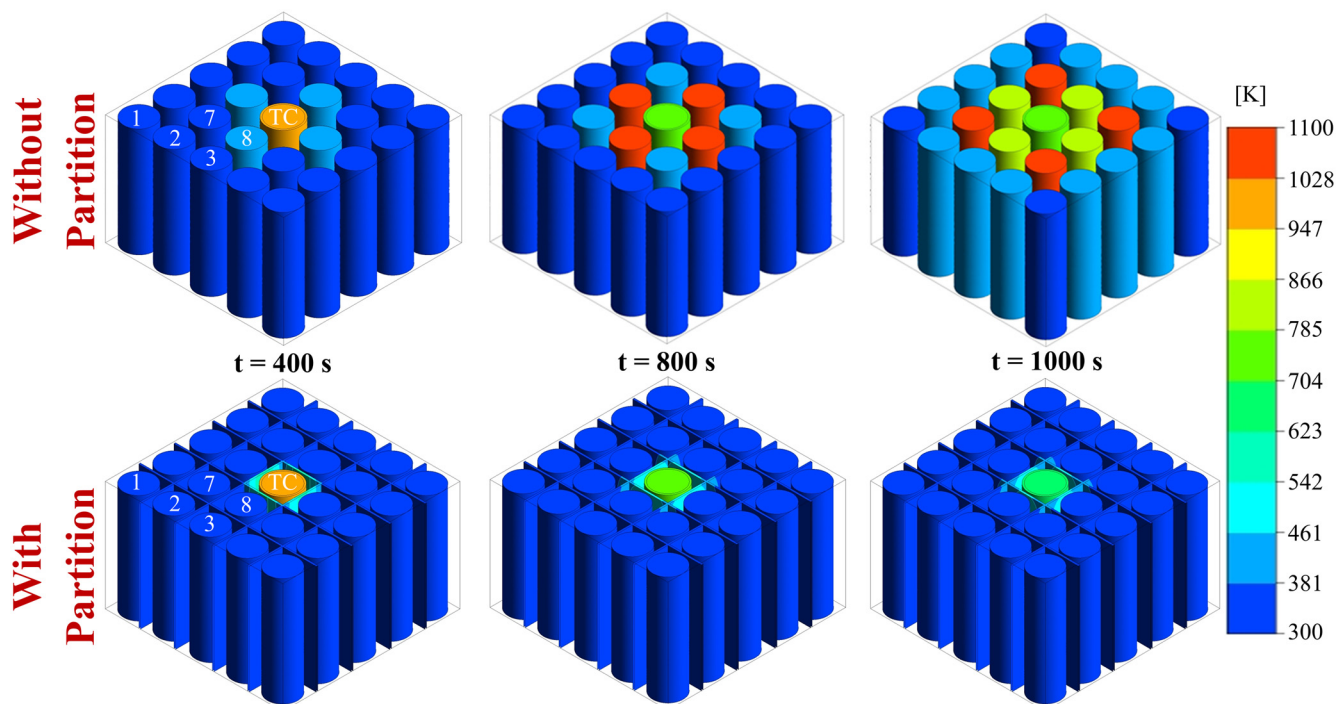

Figure 6. Effect of presence of internal partition (Simulation C): Temperature vs time plot for battery pack (a) without partition, (b) with wood partition. Problem parameters include 3 mm cell-to-cell gap, 1 mm overhead gap, 4.7×10^6 Wm^{-3} heat generation in heater up to 500 s, $\varepsilon_p = 1$, $\varepsilon_c = 0.1$.

inflexion in the trigger cell curve at t = 500 s, corresponding to the termination of sleeve heating, and at around t = 815 s and t = 910 s, when heat generated by thermal runaway in neighboring cells cause small bumps in the trigger cell curve.

Even though the internal partition may absorb significant heat from the trigger cell, as demonstrated above, it is important for this heat to be transported away from the batteries in the pack, otherwise the internal partition will simply re-emit the heat back to the trigger cell and neighboring cells. High thermal conductivity of the partition material may enable conduction of heat to the outer box, from where, heat may be removed to the ambient via convection. A set of simulations (Simulation D) are carried out to understand the impact of thermal conductivity of the partition on thermal runaway

characteristics. In these simulations, 4.5×10^6 Wm^{-3} internal heat generation up to 300 s is considered in the sleeve heater. Two different partition materials—wood and aluminum—are considered. Cell emissivity is are taken to be $\varepsilon_c = 0.1$, while that of wood and aluminum is taken to be $\varepsilon_p = 1$ and $\varepsilon_p = 0.1$, respectively. Wood and aluminum are representative of low and high thermal conductivity materials, respectively, with typical values of 0.153 Wm^{-1}K^{-1} and 202.4 Wm^{-1}K^{-1}, respectively. Results are plotted in Figs. 8a and 8b respectively. Corresponding temperature contours are shown in Fig. 9, and complete videos of the evolution of the temperature field are provided as Supplementary Information. Figures 9a and 9b show that for the abuse condition considered here, both wood and aluminum are able to prevent propagation of thermal runaway to

Figure 7. Color plots to demonstrate the impact of presence of internal partition on thermal runaway propagation. The problem parameters correspond to Fig. 6.
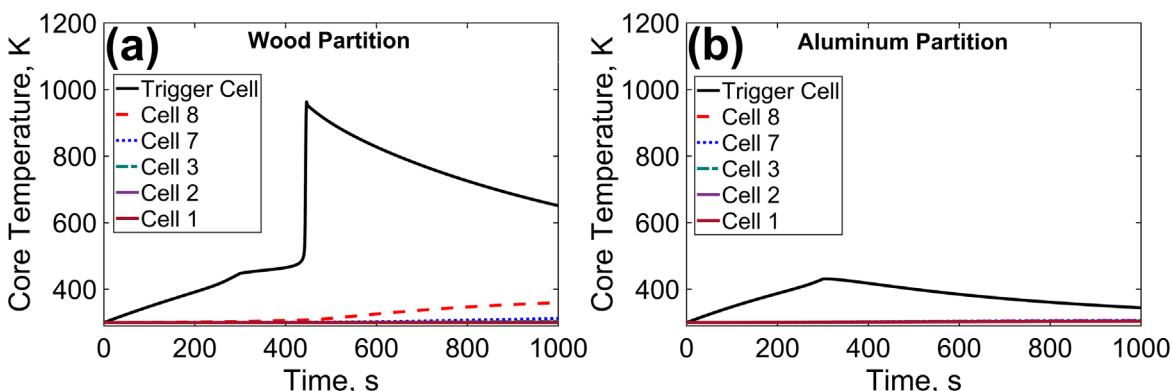
Figure 8. Effect of thermal conductivity of the internal partition material (Simulation D): Temperature vs time plot for battery pack with (a) wood partition, (b) aluminum partition. Problem parameters include 3 mm cell-to-cell gap, 1 mm overhead gap, 4.5×10^6 Wm^{-3} heat generation in heater up to 300 s, $\varepsilon_p = 1$, $\varepsilon_c = 0.1$.

neighboring cells. The outcome in the case of Aluminum partition is more desirable, as even onset in the trigger cell is prevented in this case. This is because the high thermal conductivity aluminum partition is able to diffuse away the radiative heat received from the trigger cell, and thereby preventing the onset of thermal runaway in the trigger cell altogether. Local accumulation of heat in the partition around trigger cell can be clearly seen for the case of wood partition (Fig. 9a). In contrast, heat rapidly diffuses away from the trigger cell through the partition material in the high thermal conductivity aluminum case. This also helps in rapid distribution of heat absorbed from trigger cell to a larger number of neighboring cells, which may reduce the thermal load on each neighbor, and therefore, propagation of thermal runaway. These plots show that at high thermal conductivity, the partition effectively acts like a thermal fin by providing a conduit for heat to diffuse away from the trigger cell. The higher the thermal conductivity of the partition, the more effective its performance as a fin is. An important trade-off to consider here, however, is that high thermal conductivity metals

also tend to be heavier, and, therefore, may impact the overall energy storage density of the battery pack.

Surface emissivity is the key thermal property that determines the extent of heat that is radiatively absorbed or reflected from a surface. The higher the emissivity, the higher is the rate of heat absorption, and lower is the rate of reflection of heat. The next two sets of simulations examine the impact of partition and cell emissivities on thermal runaway propagation.

First, a set of simulations (Simulation E) is carried out using wood partition with an emissivity of 0.1 and 1.0. All other parameters are held constant, including a cell emissivity of 0.1 and the sleeve heater internal heat generation rate of 4.5×10^6 Wm^{-3} up to 300 s. Results are summarized in Fig. 10 as lines plots, and in Fig. 11 as colorplots of the temperature field. Corresponding videos of the temperature distribution evolution are presented in Supplementary Information. These results show that while there is no propagation of thermal runaway in either case, it is still desirable to have high emissivity of the partition material. As shown in
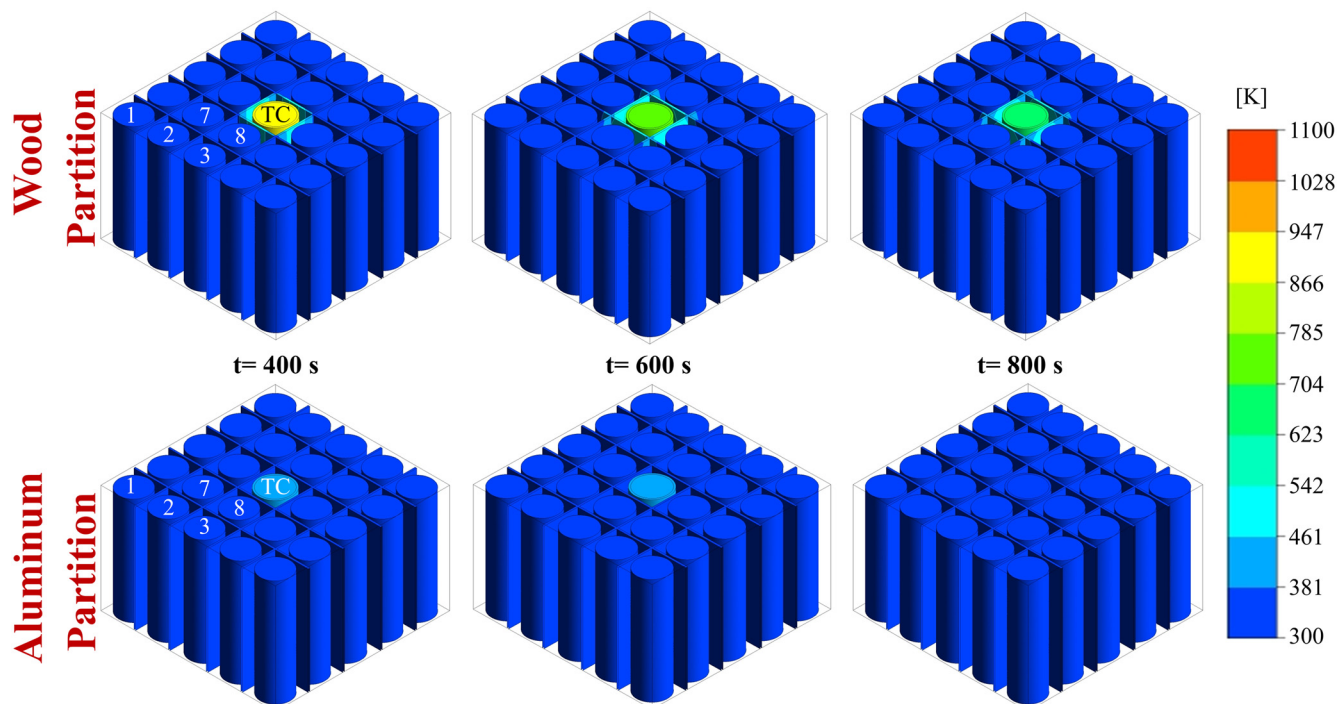
Figure 9. Color plots to demonstrate the impact of internal partition material on thermal runaway propagation. The problem parameters correspond to Fig. 8.
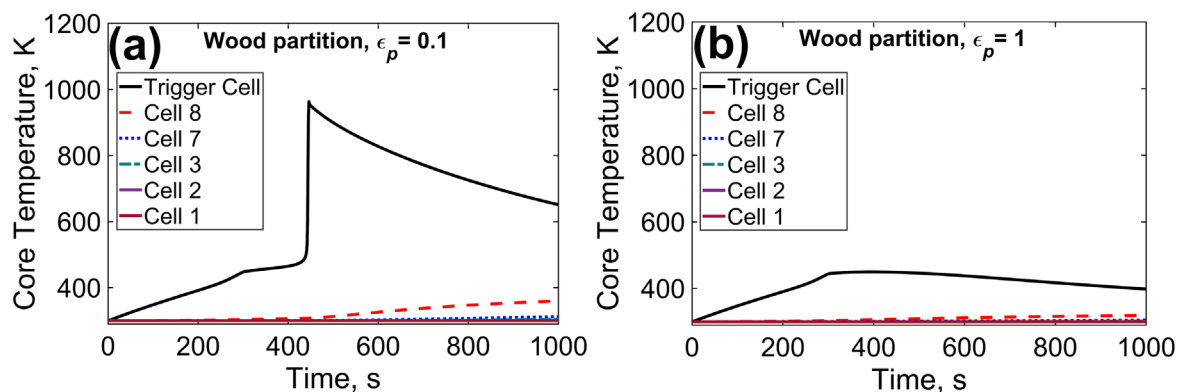

Figure 10. Effect of internal partition emissivity, ε_p (Simulation E). Temperature vs time plots for battery pack with (a) $\varepsilon_p = 0.1$; (b) $\varepsilon_p = 1$. Other problem parameters are the same as Fig. 8.

Fig. 10b, high partition emissivity enables significant heat absorption from the trigger cell, which prevents thermal runaway from occurring altogether. In the low emissivity partition case, thermal runaway does occur in the trigger cell due to insufficient absorption of heat from the trigger cell. High emissivity of the internal partition can be achieved simply by choosing a dark colored material, or by painting over with a dark colored paint. This passive, inexpensive approach may result in significant thermal benefit without adding significantly to the system weight.

It is interesting to evaluate the importance of radiative heat transfer by comparing the radiative heat flux received by the partition wall with the total heat flux received. These heat flux values are plotted in Fig. 12 as functions of time for the two cases considered in Simulation E discussed above. These plots show that radiative heat transfer peaks at the point of thermal runaway, similar to total heat transfer, and can be a significant component of total heat transfer.

Finally, the effect of emissivity of the cell on thermal runaway propagation is investigated. For this purpose, two simulations (Simulation F) with $\varepsilon_c = 1$ and $\varepsilon_c = 0.1$ are carried out. A wood

partition with emissivity of 0.1, and 1.2×10^7 Wm^{-3} heat generation in the heater up to 500 s is considered in both cases. All other parameters remain constant, as listed in Table III. High cell emissivity may be desirable to enable the trigger cell to lose as much heat as possible to prevent thermal runaway onset. However, high emissivity also results in the neighboring cells absorbing more heat from other radiative sources, such as the partition. For the purpose of minimizing radiative heat intake from neighboring sources, low emissivity may be desirable. A trade-off, therefore, clearly exists. Results presented in Figs. 13 and 14 show that for the specific thermal abuse considered here, propagation of thermal runaway does occur for both cases. However, high emissivity of cells results in somewhat delayed onset for trigger cell but faster thermal runaway propagation. This is explained on the basis of enhancement in radiative heat transfer due to increased emissivity. This increased heat transfer rate results in delayed thermal runaway onset for the trigger cell as much of the internally generated heat is emitted away. However, increased emissivity (and hence absorptivity) also results in greater heat absorption by the neighboring cells, resulting in faster propagation. On the other hand, low emissivity results in increased
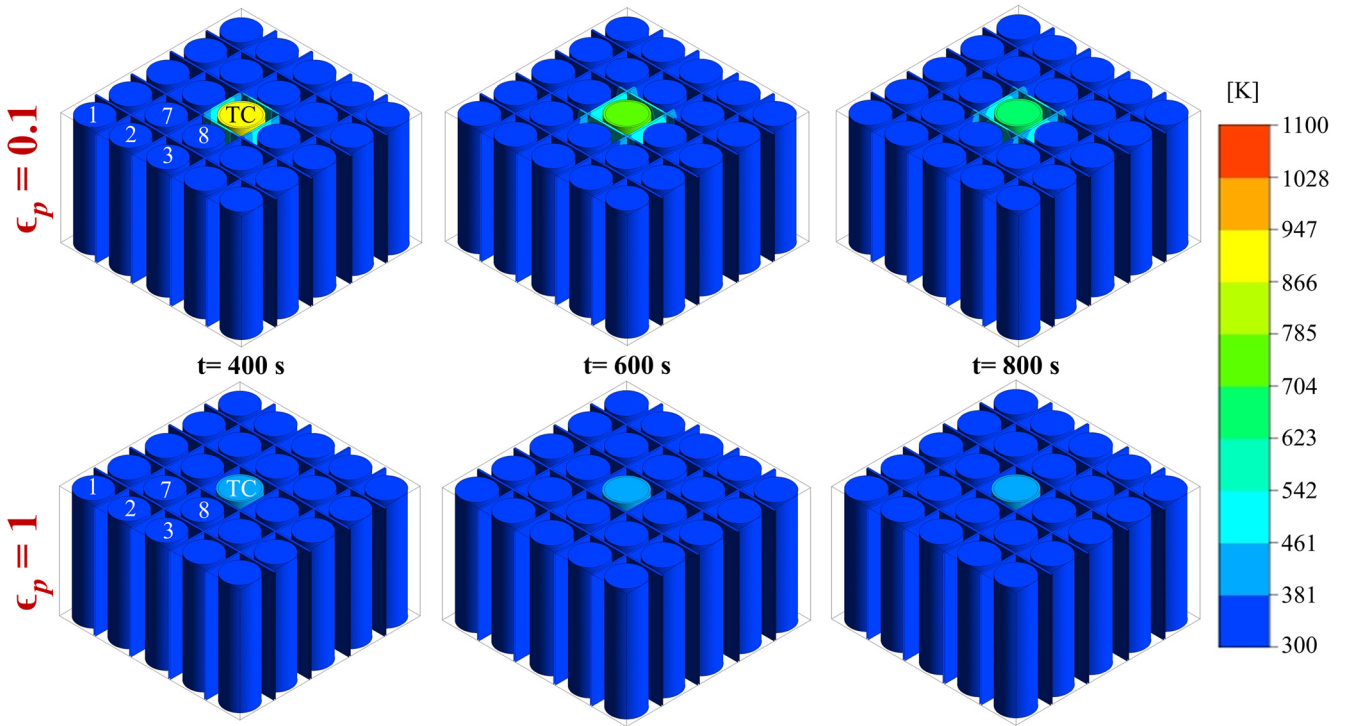
Figure 11. Color plots to demonstrate the effect of internal partition emissivity on thermal runaway propagation. The problem parameters correspond to Fig. 10.
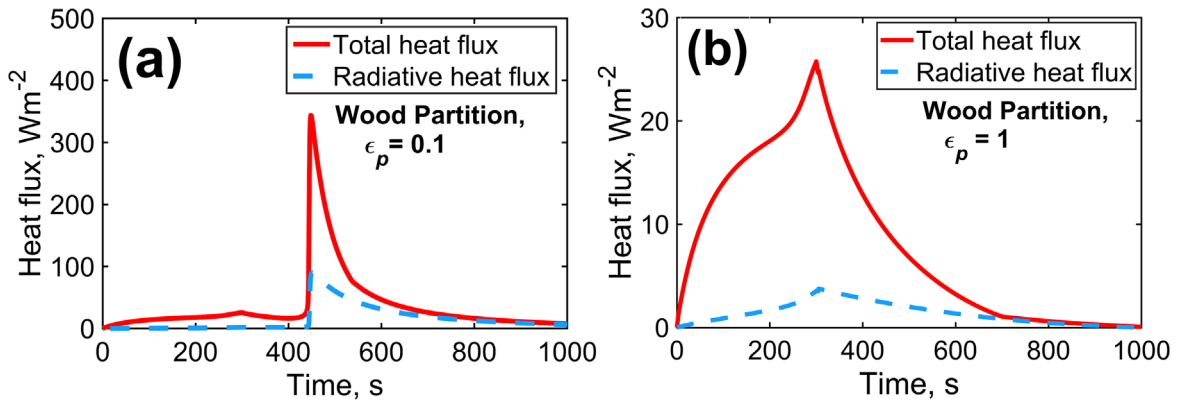

Figure 12. Comparison of radiative heat flux incident on the partition walls with total heat flux as a function of time for the two emissivity values considered in Fig. 10.
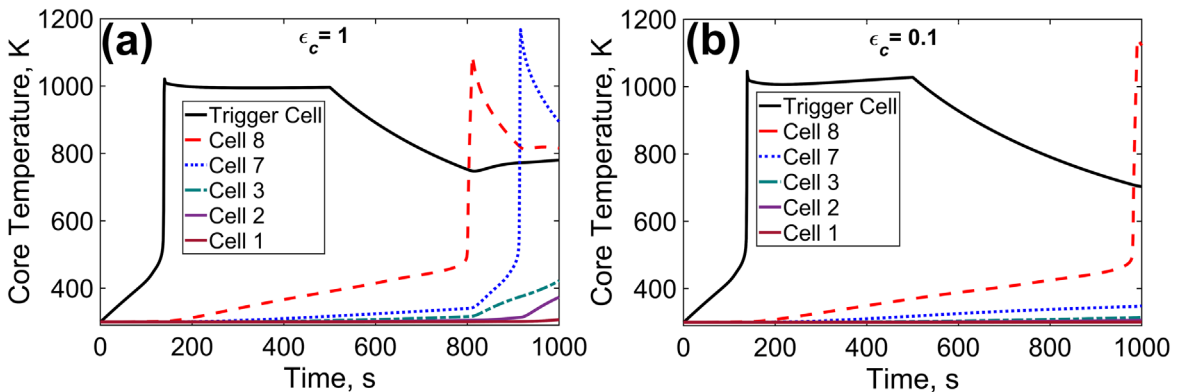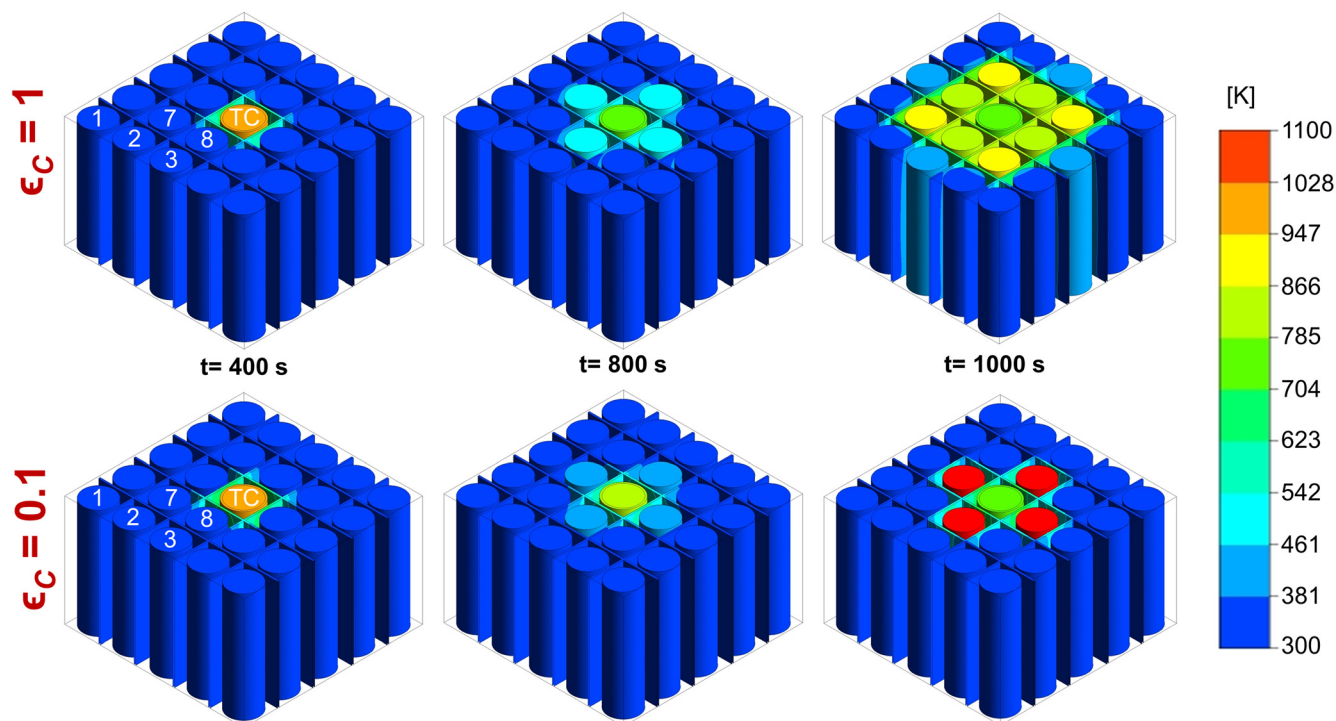

Figure 13. Effect of cell emissivity, ε_c (Simulation F): Temperature vs time plot for battery pack with (a) $\varepsilon_c = 1$, (b) $\varepsilon_c = 0.1$. Problem parameters include 3 mm cell-to-cell gap, 1.2×10^7 Wm^{-3} heat generation in heater up to 500 s, $\varepsilon_p = 0.1$.

Figure 14. Color plots to demonstrate the effect of cell emissivity on thermal runaway propagation. The problem parameters correspond to Fig. 10.

reflectivity, due to which, thermal runaway in the trigger cell occurs earlier, but propagation to neighboring cells is delayed. While this suggests possible existence of an optimal emissivity value that is neither too high nor too low, it is difficult to prescribe a universally optimal value due to the wide range of thermal abuse (for example, heat generation rate and duration) expected to be encountered in realistic conditions.

Conclusions

Thermal runaway is a considerably complicated phenomenon, the modeling of which presents several practical challenges. Given the non-linear nature of radiative heat transfer, it has often been neglected in past work, despite its likely importance at high temperatures reached during thermal runaway. By explicitly modeling radiative heat transfer through surface-to-surface view factors, this work highlights the importance of radiative heat transfer in determining the thermal fate of a battery pack. Specifically, it is shown that radiative properties of the internal partition walls in the battery pack may play a key role in determining whether the onset and propagation of thermal runaway occurs or not. This information may have practical applications in the thermal design of the battery pack. Radiative properties of the partition walls, such as emissivity, can be easily controlled, such as by painting the walls black. This represents a passive, low-cost thermal management approach that does not add to system weight. This work shows that heat transfer through the internal partition is particularly enhanced when the thermal conductivity of the partition is very high, such as for typical metals. However, the trade-off of increased weight must be carefully considered in the use of metal partition walls.

It is important to note that the present work primarily considered thermal abuse of the cell, whereas other types of abuse that may occur, such as mechanical or electrical abuse are not accounted for. Several phenomena that may occur during thermal runaway, such as cell rupture, vapor venting, combustion and flame have also been neglected. Carrying out combined modeling of such processes— each of which is highly non-linear—is an important challenge in this field.

CRediT Authorship Contribution Statement

D. Mishra—Methodology, Investigation, Visualization, Data Curation; K. Shah—Investigation, Methodology; A. Jain— Conceptualization, Methodology, Supervision, Project Administration. All authors contributed towards Writing Original Draft, Review and Editing.

ORCID

Krishna Shah https://orcid.org/0000-0002-7802-6361
Ankur Jain https://orcid.org/0000-0001-5573-0674

References

1. B. Diouf and R. Pode, *Renew. Energy*, **76**, 375 (2015).
2. D. Lisbona and T. Snee, *Process Saf. Environ. Prot.*, **89**, 434 (2011).
3. X. Feng, M. Ouyang, X. Liu, L. Lu, Y. Xia, and X. He, *Energy Storage Mater.*, **10**, 246 (2018).
4. R. Spotnitz and J. Franklin, *J. Power Sources*, **113**, 81 (2003).
5. I. Esho, K. Shah, and A. Jain, *Appl. Therm. Eng.*, **145**, 287 (2018).
6. T. Yokoshima, F. Maeda, T. Osaka, K. Takazawa, S. Egusa, S. Naoi, S. Ishikura, and K. Yamamoto, *J. Power Sources*, **393**, 67 (2018).
7. L. Huang, Z. Zhang, Z. Wang, L. Zhang, X. Zhu, and D. D. Dorrell, *J. Energy Storage*, **25**, 100811 (2019).
8. A. W. Golubkov, S. Scheikl, R. Planteu, G. Voitic, H. Wiltsche, C. Stangl, G. Fauler, A. Thaler, and V. Hacker, *RSC Adv.*, **5**, 57171 (2015).
9. D. Ren, X. Feng, L. Liu, H. Hsu, L. Lu, L. Wang, X. He, and M. Ouyang, *Energy Storage Mater.*, **34**, 563 (2021).
10. D. Mishra and A. Jain, *J. Electrochem. Soc.*, **168**, 020504 (2021).
11. D. Mishra, K. Shah, and A. Jain, *J. Electrochem. Soc.*, **168**, 060555 (2021).
12. R. Srinivasan et al., *J. Electrochem. Soc.*, **167**, 020559 (2020).
13. C. F. Lopez, J. A. Jeevarajan, and P. P. Mukherjee, *J. Electrochem. Energy Convers. Storage*, **13**, 031007 (2016).
14. P. T. Coman, E. C. Darcy, C. T. Veje, and R. E. White, *Appl. Energy*, **203**, 189 (2017).
15. C. Lee, A. O. Said, and S. I. Stoliarov, *Transp. Res. Rec.*, **2673**, 408 (2019).
16. D. Ouyang, J. Liu, M. Chen, J. Weng, and J. Wang, *Appl. Sci.*, **8**, 1263 (2018).
17. X. He, Z. Hu, F. Restuccia, H. Yuan, and G. Rein, *Appl. Therm. Eng.*, **197**, 117349 (2021).

18. X. Liu, Z. Wu, S. I. Stoliarov, M. Denlinger, A. Masias, and K. Snyder, *J. Electrochem. Soc.*, **165**, A2909 (2018).
19. F. Larsson, J. Anderson, P. Andersson, and B.-E. Mellander, *J. Electrochem. Soc.*, **163**, A2854 (2016).
20. X. Feng, X. He, M. Ouyang, L. Lu, P. Wu, C. Kulp, and S. Prasser, *Appl. Energy*, **154**, 74 (2015).
21. C. Yuan, Q. Wang, Y. Wang, and Y. Zhao, *Appl. Therm. Eng.*, **153**, 39 (2019).
22. C. Lee, A. O. Said, and S. I. Stoliarov, *J. Electrochem. Soc.*, **167**, 090524 (2020).
23. S. Wilke, B. Schweitzer, S. Khateeb, and S. Al-Hallaj, *J. Power Sources*, **340**, 51 (2017).
24. A. O. Said and S. I. Stoliarov, *Fire Saf. J.*, **121**, 103296 (2021).
25. T. Liu, J. Hu, C. Tao, X. Zhu, and X. Wang, *Fire Saf. J.*, **120**, 103117 (2021).
26. A. O. Said, A. Garber, Y. Peng, and S. I. Stoliarov, *Fire Technol.*, **57**, 1 (2021).
27. K. S. Kshetrimayum, Y.-G. Yoon, H.-R. Gye, and C.-J. Lee, *Appl. Therm. Eng.*, **159**, 113797 (2019).
28. W. Zhang, Z. Liang, X. Yin, and G. Ling, *Appl. Therm. Eng.*, **184**, 116380 (2021).
29. K. Xu, M. S. Ding, S. Zhang, J. L. Allen, and T. R. Jow, *J. Electrochem. Soc.*, **149**, A622 (2002).
30. Y. E. Hyung, D. R. Vissers, and K. Amine, *J. Power Sources*, **119–121**, 383 (2003).
31. D. H. Doughty, E. P. Roth, C. C. Crafts, G. Nagasubramanian, G. Henriksen, and K. Amine, *J. Power Sources*, **146**, 116 (2005).
32. B. K. Mandal, A. K. Padhi, Z. Shi, S. Chakraborty, and R. Filler, *J. Power Sources*, **161**, 1341 (2006).
33. M. C. Niculuță and C. Veje, *J. Phys. Conf. Ser.*, **395**, 012013 (2012).
34. W. Allafi, C. Zhang, K. Uddin, D. Worwood, T. Quang, D. Pedro, A. Ormeno, K. Li, and J. Marco, *Appl. Therm. Eng.*, **143**, 472 (2018).
35. T. D. Hatchard, D. D. MacNeil, D. A. Stevens, L. Christensen, and J. R. Dahn, *Electrochem. Solid-State Lett.*, **3**, 305 (2000).
36. C. F. Lopez, J. A. Jeevarajan, and P. P. Mukherjee, *J. Electrochem. Soc.*, **162**, A1905 (2015).
37. G. H. Kim, A. Pesaran, and R. Spotnitz, *J. Power Sources*, **170**, 476 (2007).
38. M. Parhizi, M. B. Ahmed, and A. Jain, *J. Power Sources*, **370**, 27 (2017).
39. S. J. Drake, D. A. Wetz, J. K. Ostanek, S. P. Miller, J. M. Heinzel, and A. Jain, *J. Power Sources*, **252**, 298 (2014).
40. M. Parhizi, M. Ahmed, and A. Jain, *J. Power Sources*, **370**, 27 (2017).
41. M. F. Couturier, K. George, and M. H. Schneider, *Wood Sci. Technol.*, **30**, 179 (1996).
42. J. R. Howell, M. P. Mengüç, K. Daun, and R. Siegel, *Thermal Radiation Heat Transfer* (CRC press, Boca Raton, FL) (2020).
43. T. Walker, S. C. Xue, and G. W. Barton, *J. Heat Transfer*, **132**, 1 (2010).